# Alignment of ferroelectric polarization and defect complexes in copper-doped potassium niobate

Sabine Körbel* and Christian Elsässer†

*Fraunhofer Institute for Mechanics of Materials IWM, Wöhlerstraße 11, 79108 Freiburg, Germany*

(Received 22 April 2013; revised manuscript received 15 November 2013; published 27 December 2013)

Defect complexes consisting of Cu substitutionals on Nb sites and oxygen vacancies in potassium niobate, $KNbO_3$, are investigated with respect to their contribution to ferroelectric hardening by means of density-functional theory and classical atomistic simulations. We determine the easy and hard directions for the ferroelectric polarization created by these defect complexes, the energy differences between easy and hard directions, and upper limits for the energy barriers for switching the ferroelectric polarization between these directions. The ferroelectric polarization preferentially aligns with the defect complexes, which is expected to impede polarization switching and hence to contribute to ferroelectric hardening.

DOI: 10.1103/PhysRevB.88.214114 PACS number(s): 61.72.−y, 71.15.Mb, 77.80.Fm, 77.84.Ek

## I. INTRODUCTION

In the context of ongoing efforts to replace lead-containing materials by more environment-friendly ones in industrial production, lead-free ferroelectrics, such as potassium sodium niobate, or bismuth sodium titanate, are currently considered for use in piezoelectric actuators or sensors.[1] In ferroelectrics, the piezoelectric effect can be much stronger than in piezoelectrics like quartz without spontaneous polarization.[2] In order to obtain a strong and nearly linear response of the mechanical strain $\epsilon$ on the electric field $E$ for an actuator, or vice versa of the electric polarization $P$ on the mechanical stress $\sigma$ for a sensor, a ferroelectric oxide can be "hardened" by acceptor doping. Acceptor dopants in ferroelectric oxides are substitutional cations which can attract oxygen vacancies for charge compensation and thus form defect dipoles. It is generally believed that these dipoles contribute to ferroelectric hardening by impeding the motion of ferroelectric domain walls.[2] In Ref. 3, it was proposed that defect dipoles in aged hard ferroelectrics can provide a restoring force for the ferroelectric polarization and thus enable reversible domain switching by 90°, which is accompanied by a large strain. According to Ref. 3, this 90° domain switching mechanism works as follows: the defect dipoles in an acceptor-doped ferroelectric align with the polarization in each ferroelectric domain after some time. If initially no external electric field is present, the polarization directions of the ferroelectric domains are statistically distributed. Once an external electric field is applied, a fraction of the domains is initially oriented perpendicular to the direction of the external electric field. In the presence of an external electric ac field, the polarization in these domains aligns with the electric field, whereas the defect dipoles do not have enough time to reorient, resulting in a large strain of these domains parallel to the electric field. Whereas without defect complexes this large strain normally occurs just once, because the new domain configuration is energetically equivalent to the old one, defect complexes can restore the initial polarization direction of the domains so that the reorientation process becomes reversible. If the initial polarization of the material was macroscopically zero, the defect complexes will restore the initial domain configuration each time the external electric ac field crosses zero, and a constricted $P$-$E$ curve or "double-hysteresis" loop is measured. Such double-hysteresis loops were indeed observed in several acceptor-doped ferroelectric perovskites, e.g., in $BaTiO_3$ doped with Fe,[3] in Mn-doped $Pb(Ti,Zr)O_3$,[4] and in Mn- and Cu-doped $(K,Na)NbO_3$.[4–6]

On the atomic level, two mechanisms of ferroelectric hardening caused by defect dipoles are possible: (1) in the presence of the defect dipole some polarization directions become energetically unfavorable, which impedes switching the polarization into these directions, or (2) the defect dipoles create or increase energy barriers for switching between different polarization directions. Of course, both mechanisms may occur simultaneously as well. In order to enable reversible 90° domain switching, the energy barrier for polarization switching must be lower than that for rotating the defect complexes.

It is the purpose of this work to investigate on the atomic level, using the example of Cu-doped $KNbO_3$, whether defect complexes provide these conditions. Potassium niobate, $KNbO_3$, was chosen because it is an end member of the solid solution system potassium sodium niobate, $K_{0.5}Na_{0.5}NbO_3$ (KNN), and it has the same perovskite structure as KNN.[7] KNN is regarded as a promising lead-free substitute for today's best material, lead zirconate titanate, $Pb(Zr,Ti)O_3$ (PZT), because in some cases for KNN similarly good piezoelectric properties as for PZT have been observed.[8] CuO is often added during fabrication as a sintering aid,[9] and Cu is apparently incorporated into the KNN lattice.[5,6] In electron paramagnetic resonance (EPR) spectroscopy experiments of Cu-doped $KNbO_3$ and KNN, evidence for two types of defect complexes was found, and these two defect complexes were identified as $Cu_{Nb}$-$V_O$ and $V_O$-$Cu_{Nb}$-$V_O$.[10,11]

$KNbO_3$ exists in several ferroelectric phases depending on the temperature, analogous to $BaTiO_3$.[12,13] In the orthorhombic room-temperature phase of $KNbO_3$, the ferroelectric polarization is approximately directed along one of the 12 ⟨110⟩ directions of the primitive unit cell (the orthogonal components are one order of magnitude smaller[12]), which are all equivalent in the perfect crystal structure. The primitive unit cell of orthorhombic $KNbO_3$ is very similar to the cubic one, the difference being a small elongation (approximately 2% of the cubic lattice parameter) of the unit-cell edges along one of the ⟨110⟩ directions and small mutual atomic displacements (approximately 4%) along the same direction in the orthorhombic phase. In the presence of defect complexes, some of the ⟨110⟩ directions of the ferroelectric polarization

 

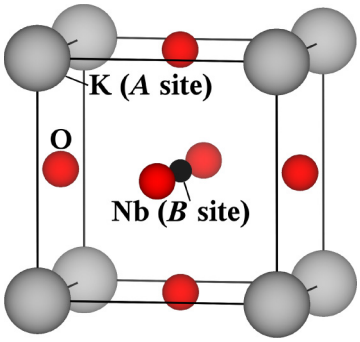


FIG. 1. (Color online) A cubic unit cell of the perovskite structure of $KNbO_3$.

become inequivalent. A cubic unit cell of $KNbO_3$ is depicted in Fig. 1(a).

In this work, we proceed as follows: At first we determine formation energies of atomic defects and binding energies of defect complexes consisting of Cu substitutionals on Nb sites ($Cu_{Nb}$) and oxygen vacancies ($V_O$) in $KNbO_3$ [cf. Figs. 2(a) and 2(b)] in order to confirm that these defect complexes are energetically favorable. The defect formation energies are calculated in the cubic, paraelectric phase, which occurs at the high temperatures at which $KNbO_3$ and KNN ceramics are typically fabricated.[14] Then, we estimate the energy barrier for reorienting the defect dipole $Cu_{Nb}$-$V_O$ in order to confirm that this is higher than the one for reorienting the ferroelectric polarization. At last, we investigate whether the defect complexes stabilize or destabilize some orientations of the ferroelectric polarization in the orthorhombic room-temperature phase (hardening mechanism 1), and how they affect energy barriers for switching the spontaneous ferroelectric polarization (hardening mechanism 2) for a given fixed orientation of the defect complex.

## II. COMPUTATIONAL METHODOLOGY

At first, in order to determine the thermodynamic stability of the defect complexes, the formation energies of the $Cu_{Nb}$-$V_O$ and a straight form of the $V_O$-$Cu_{Nb}$-$V_O$ defect [see Figs. 2(a) and 2(b)], are calculated using density-functional theory (DFT). In a second step, for a given orientation of such a defect complex, the energies of different orientations of the surrounding ferroelectric polarization are calculated also with DFT. In Fig. 2, these different relative orientations of the ferroelectric polarization with respect to the defect complexes are depicted. Two variants, a straight and a bent one, of the ($V_O$-$Cu_{Nb}$-$V_O$) defect complex [cf. Figs. 2(b) and 2(c)] are considered. In principle, the possibility that Cu substitutes on K sites can not be excluded. However, in a previous work, we found that the most stable configuration in thermal equilibrium at room temperature is the substitution on Nb sites.[15] In a third step, the energies thus obtained with DFT are used as target data for validating a classical interatomic potential for Cu-doped $KNbO_3$. At last, this potential is applied to obtain energy barriers for switching between the different polarization directions in order to reduce the number of computationally expensive DFT calculations needed.

### A. Formation of defect complexes in cubic $KNbO_3$

#### 1. Defect formation energies

Using density-functional theory (DFT), the formation energies $E^f$ of the defect complexes are calculated following the approach outlined, e.g., in Ref. 16:

$$E^f[X^q] = E_{tot}[X^q] - E_{tot}[\text{bulk}] - \sum_i \mu_i n_i + q(E_F + E_{VBM}). \quad (1)$$

Here, $E_{tot}[X^q]$ is the total energy of the supercell with a defect $X$ carrying a charge $q$, $E_{tot}$[bulk] is the total energy of a perfect supercell of the same size, $\mu_i$ is the chemical potential of atom species $i$, $n_i$ is the number of atoms of species $i$ that are exchanged with a reservoir in order to incorporate the defect into the crystal, and $E_F$ is the Fermi energy or chemical potential of the electrons relative to the valence-band maximum $E_{VBM}$.[16] A potential alignment correction is added to $E_{VBM}$ in order to account for the difference of the energy zero between the system with and without a defect.[16]

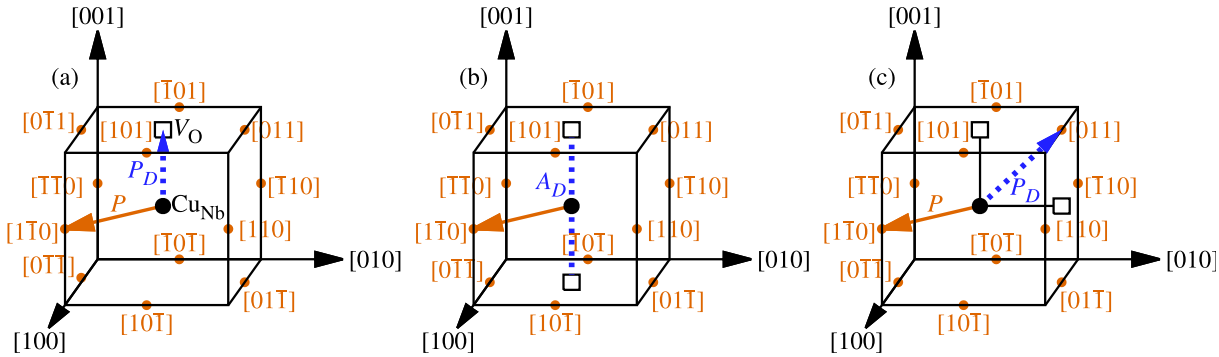


FIG. 2. (Color online) Defect complex configurations of $Cu_{Nb}$ (black circle) and $V_O$ (small black square) in a unit cell of orthorhombic ferroelectric $KNbO_3$ with different orientations of the ferroelectric polarization $P$. (a) $Cu_{Nb}$-$V_O$; (b) straight $V_O$-$Cu_{Nb}$-$V_O$; (c) bent $V_O$-$Cu_{Nb}$-$V_O$. The dashed blue arrows mark the electric dipole moments of the defects $P_D$, dashed blue lines the defect axes $A_D$, and the orange dots mark the possible directions of the spontaneous ferroelectric polarization $P$ in the orthorhombic phase (they do not mark atoms). One polarization direction is indicated by a solid orange arrow.

The chemical potentials of metal atoms are approximated by the total energy per atom in the crystalline reference phases, so that the formation enthalpies are approximated by formation energies. For the oxygen gas, however, a temperature and pressure correction based on the equation of state of the ideal gas is applied following Ref. 17:

$$\begin{aligned}\mu_{\mathrm{O}}(T,p) &= \frac{1}{2}G_{\mathrm{O}_2}(T,p)\\ &= \frac{1}{2}[H_{\mathrm{O}_2}(T,p_0) - TS_{\mathrm{O}_2}(T,p_0)]\\ &\quad + \frac{1}{2}k_BT\ln\left(\frac{p}{p_0}\right)\\ &= \mu_{\mathrm{O}}(T,p_0) + \frac{1}{2}k_BT\ln\left(\frac{p}{p_0}\right),\end{aligned} \tag{2}$$

where $p_0$ is a reference oxygen partial pressure (the standard atmospheric pressure, about 1 bar), $T$ is the temperature, $G$ is the Gibbs free energy per molecule, and $H$ and $S$ are enthalpy and entropy per oxygen molecule, which can be found in thermochemical tables and are taken from Ref. 18.

The total energy of the oxygen molecule, needed to obtain the chemical potential of gaseous oxygen, is calculated in a periodic cubic supercell with an edge length of about 30 Å. For the oxygen molecule, spin polarization is taken into account.

The chemical potentials are chosen such that they lie in the range of thermodynamic stability of $KNbO_3$. After introducing relative chemical potentials $\Delta\mu_i$ with respect to those in the most stable elemental phase of each species $\mu_i^0$,

$$\Delta\mu_i = \mu_i - \mu_i^0, \tag{3}$$

the condition that $KNbO_3$ be stable with respect to decomposition into competing phases is

$$\Delta\mu_{\mathrm{K}} + \Delta\mu_{\mathrm{Nb}} + 3\Delta\mu_{\mathrm{O}} = \Delta H_f^0(\mathrm{KNbO_3}), \tag{4}$$

where $\Delta H_f^0(\mathrm{KNbO_3})$ is the formation enthalpy of $KNbO_3$ from its elemental constituents (metallic K, metallic Nb, and gaseous oxygen). The equality in Eq. (4) means that $KNbO_3$ is in equilibrium with the reservoirs of its constituents.

An upper boundary of the chemical potentials is given by

$$\Delta\mu_i \leqslant 0 \tag{5}$$

since otherwise the elemental phase of component $i$ would precipitate. Other possible competing phases lead to further constraints for the chemical potentials:

$$\begin{aligned}2\Delta\mu_{\mathrm{K}} + \Delta\mu_{\mathrm{O}} &\leqslant \Delta H_f^0(\mathrm{K_2O}),\\ 2\Delta\mu_{\mathrm{K}} + 2\Delta\mu_{\mathrm{O}} &\leqslant \Delta H_f^0(\mathrm{K_2O_2}),\\ \Delta\mu_{\mathrm{Nb}} + \Delta\mu_{\mathrm{O}} &\leqslant \Delta H_f^0(\mathrm{NbO}),\\ \Delta\mu_{\mathrm{Nb}} + 2\Delta\mu_{\mathrm{O}} &\leqslant \Delta H_f^0(\mathrm{NbO_2}),\\ 2\Delta\mu_{\mathrm{Nb}} + 5\Delta\mu_{\mathrm{O}} &\leqslant \Delta H_f^0(\mathrm{Nb_2O_5}).\end{aligned} \tag{6}$$

The remaining region of chemical potentials for which $KNbO_3$ is stable is depicted in Fig. 3.

The chemical potentials chosen for the following are those of point 1 in Fig. 3, so that the defect formation energies are calculated for oxygen-rich conditions (air) at a temperature well above room temperature, but below a typical sintering temperature for this compound [about 1300 K (Ref. 14)]. The chemical potential of Cu is set to $\Delta\mu_{\mathrm{Cu}} = \Delta H_f^0(\mathrm{CuO}) - \Delta\mu_{\mathrm{O}}$. The binding energies of the defect complexes are independent of the chemical potentials of the elements.

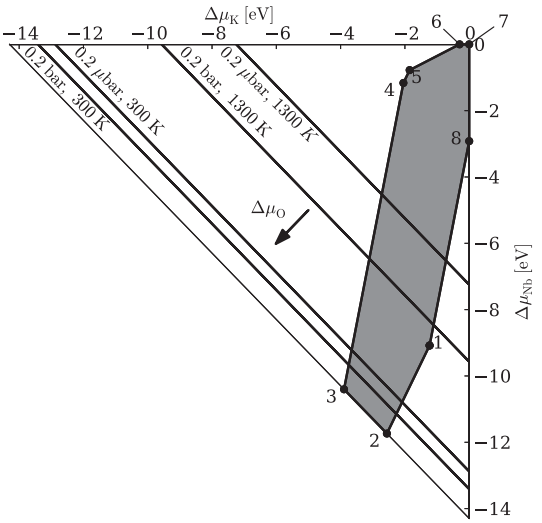


FIG. 3. Region of possible values for the relative chemical potentials as defined in Eq. (3). The area inside the outer triangle is given by the Eqs. (4) and (5), the shaded area remains after taking into account Eqs. (6). The diagonal lines indicate the chemical potentials of oxygen that correspond to oxygen partial pressures in air at the standard atmospheric pressure and in air at $10^{-6}$ bar, for the temperatures 300 and 1300 K (Ref. 15).

### 2. Charge corrections

In various studies published in the literature, the convergence of defect formation energies with respect to supercell size has been improved substantially by applying a classical scheme that accounts for defect-defect and defect-jellium interactions in the case of charged defects. This correction, based on the work of Makov and Payne,[19] consists of calculating the classical electrostatic energy of a periodic array of point charges in a compensating homogeneous charge background or jellium with an effective dielectric constant and by subtracting this energy from the total energy of the supercell. Typically, the first two or three terms of a multipole expansion (monopole, dipole, and quadrupole terms) are corrected for in this scheme. For cubic systems, the correction is[19]

$$E = E_0 - \frac{q^2\alpha}{2\varepsilon L} - \frac{2\pi p^2}{3\varepsilon V} - \frac{2\pi Qq}{3\varepsilon L^3} + \mathcal{O}(L^{-5}), \tag{7}$$

where $E$ is the formation energy of the periodic array of atomic defects, $E_0$ the one of the isolated defect of interest, $q$ the defect charge, $\alpha$ the Madelung constant for the given geometry, $\varepsilon$ the dielectric constant, $p$ the defect dipole moment, $Q$ the quadrupole moment, $V$ the supercell volume, and $L$ the effective length of the supercell, for example $V^{1/3}$. For noncubic systems, the expression for the dipole-dipole energy [the third term on the right of Eq. (7)] has to be modified.[20] However, as pointed out in Ref. 21, this correction is an upper limit. The more delocalized the defect charge, the

smaller the correction and the higher the needed multipole orders that should be taken into account. In the case of cubic $KNbO_3$, a practical complication occurs when choosing the dielectric constant. The dielectric constant in the cubic phase is strongly temperature dependent (at the cubic-tetragonal phase transition it assumes a maximum)[22] and can not simply be extrapolated to the zero temperature of the calculation. In principle, the validity of the Makov-Payne correction (including the choice of the dielectric constant and the number of multipole orders taken into account) can be assessed by a convergence study of the corrected defect formation energies with respect to the supercell size and shape, possibly taking into account a change in dielectric constant near the defect as in Ref. 23. Such a systematic study is not done here, only an estimate of the monopole-monopole and dipole-dipole energy without convergence study is given in the results section. The formation energies shown there are those without correction.

In the cubic high-temperature phase, for which we calculate the defect formation energies, the dielectric constant is isotropic, and the monopole-monopole and dipole-dipole terms are given by the first two terms of Eq. (7). In $KNbO_3$ in the orthorhombic phase at room temperature, the dielectric tensor is anisotropic, and we calculate the monopole-monopole energy using the Ewald summation expression for the screened Madelung constant $\alpha_\varepsilon$ from Ref. 24, which is derived in Ref. 25. Using $\alpha_\varepsilon$, we calculate the dipole-dipole term as the Madelung energy of a lattice of dipoles minus the binding energy of a dipole.

The dielectric constant of $KNbO_3$ in the cubic phase is estimated from Fig. 2 of Ref. 22 to be at least about 2500 in the studied temperature range (up to 460 °C). This value of 2500 is used to estimate the monopole-monopole energy in the cubic phase. For the orthorhombic phase, the clamped dielectric constant tensor measured by Wiesendanger[26] is used. In the principal-axes system, it reads as diag(37,780,24), where the polarization is oriented along the third axis.

### B. Details of the DFT calculations

Using DFT for structural relaxations of systems that are not very small, the most obvious choice for the exchange-correlation potential is either a local-density approximation (LDA) or a generalized-gradient approximation (GGA). In Ref. 27, structural properties of $KNbO_3$ obtained with LDA, GGA, and a weighted-density approximation are compared. Whereas the LDA result for the lattice constant deviates from the experimental one more strongly than the GGA result, a clear advantage of the GGA for the atomic displacements and the ferroelectric instabilities, which we are mainly interested in, is not obvious. Therefore, we choose the simpler LDA.

For the DFT calculations in this work, the Ceperley-Alder[28] LDA exchange-correlation functional as parametrized by Perdew and Zunger[29] and a mixed basis of plane waves and atom-centered basis functions[30–34] for K $s + p$ semicore states, O $p$ valence states, Nb $s + p$ semicore and $d$ valence states, and Cu $d$ valence states are used. The atom-centered basis functions account for strongly localized orbitals, such as $d$ orbitals, and accelerate in general the convergence with respect to the plane-wave cutoff energy compared to a pure plane-wave basis. The atomic cores are represented by optimally smooth[35] norm-conserving pseudopotentials.

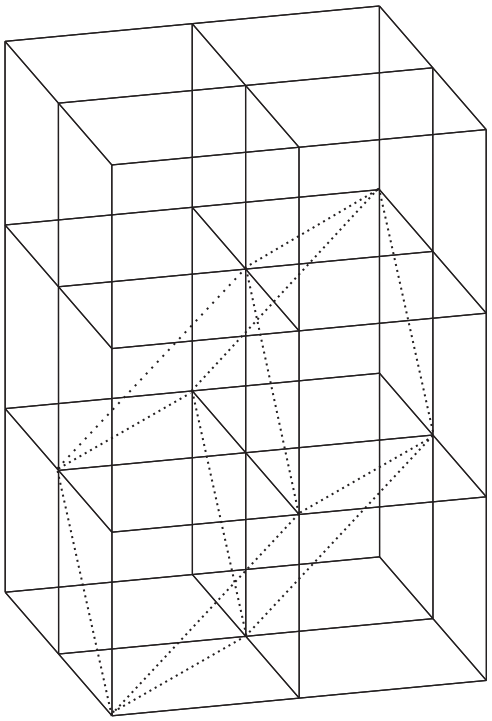

FIG. 4. A $2 \times 2 \times 3$ simple-cubic supercell used in the calculation of defect formation energies in cubic $KNbO_3$ (solid lines mark the edges of the single simple cubic perovskite unit cells). The dotted line marks the edge of a single face-centered-cubic (fcc) or face-centered-orthorhombic (fco) unit cell, which contains two formula units of $KNbO_3$. A $2 \times 2 \times 2$ supercell of the fco unit cell shown here is chosen for orthorhombic $KNbO_3$.

The defect formation energies are calculated with supercells consisting of $2 \times 2 \times 3$ simple cubic (sc) perovskite unit cells (60 atoms) at the calculated equilibrium lattice constant of cubic $KNbO_3$ ($a = 3.943$ Å). The supercell is depicted in Fig. 4. Spin polarization is neglected here. Test calculations for isolated Cu substitutionals in (K,Na)$NbO_3$ including spin polarization yield energy differences of about 0.2 eV between the polarized and the unpolarized states, and in orthorhombic $KNbO_3$ with defect complexes we obtain energy differences of 0.1 eV ($Cu_{Nb}$-$V_O$) and 0.07 eV ($Cu_{Nb}$-$2V_O$), thus the spin polarization of the Cu defects has only a small effect on the defect formation energies.

A plane-wave cutoff energy of 340 eV and a $4 \times 4 \times 3$ Monkhorst-Pack[36] $k$-point mesh with Gaussian broadening[37] by 0.2 eV are applied. This $k$-point mesh corresponds approximately to a $8 \times 8 \times 8$ $k$-point mesh for the single perovskite unit cell, which has been found to be sufficiently dense to obtain well-converged properties of ferroelectric $KNbO_3$ in previous studies by other authors (e.g., Ref. 38).

For total-energy calculations, charged atomic defects are accounted for by applying a compensating homogeneous charge background. In all cases, the atomic positions are relaxed until the forces are smaller than 10 meV/Å.

#### 1. Time scales for the formation of defect complexes

In Ref. 39, the time scales for the formation and alignment of defect dipoles have been determined by means of a kinetic model in the case of Cu- and Fe-doped lead titanate. Their approach is based on the Arlt–von Neumann model (cf. Ref. 40 and references therein), which describes the buildup of an internal bias field caused by the alignment of defect dipoles and the ferroelectric polarization in an external electric field in terms of rate equations for the jumps of oxygen vacancies. In Ref. 39, the energy barriers needed for the rate equations have been determined *ab initio* for all possible jumps, and it has been found that at temperatures between the Curie temperature and room temperature the equilibrium distribution of the oxygen vacancies is reached within seconds. Here, we follow a related, but simpler approach to estimate the equilibration time for oxygen vacancies in Cu-doped $KNbO_3$. Using the Einstein relation,[41] the diffusion constant $D$ of a given species in cubic crystals is

$$D = \langle R^2 \rangle / 6t, \tag{8}$$

where $\langle R^2 \rangle$ is the averaged quadratic diffusion length after a time $t$. According to classical transition-state theory,[42] the diffusion constant can be written as

$$D = N_{\mathrm{NN}} \nu_a e^{(E_{\mathrm{barrier}}/k_B T)} \lambda^2 f / 6, \tag{9}$$

where $N_{\mathrm{NN}}$ is the number of nearest-neighbor sites of the diffusing species, and $\nu_a$ is the attempt frequency for jumps, which we approximate, following Ref. 43, by the lowest optical phonon frequency of 190 $\mathrm{cm}^{-1}$ or $\nu_a = 0.9$ THz obtained experimentally for $KNbO_3$,[44] $\lambda$ is the distance to that neighboring lattice site, $f$ is a correlation factor which accounts for deviations of the diffusion behavior from a random walk, and $E_{\mathrm{barrier}}$ is the energy barrier for the jump. According to Ref. 42, an approximation for the correlation factor $f$ is $f = (1 - 1/N_{\mathrm{NN}})/(1 + 1/N_{\mathrm{NN}})$, where $N_{\mathrm{NN}}$ is the number of nearest-neighbor lattice sites. In the perovskite structure, $N_{\mathrm{NN}}$ is 8 for the oxygen atoms, so that $f = 0.778$. Assuming a random walk of the oxygen vacancies, the average number of jumps a vacancy needs to encounter a Cu substitutional is given by $\langle N_{\mathrm{jump}} \rangle = 1/p_{\mathrm{Cu}}$, where $p_{\mathrm{Cu}}$ is the probability that a given lattice site is a nearest neighbor of a Cu substitutional. The experimental Cu concentration of $c_{\mathrm{Cu}} = 0.25$ mol% used in Ref. 11 is assumed also here. For the average number of hops, a vacancy needs to end up next to a Cu substitutional, the corresponding diffusion length is $R = \sqrt{\langle N_{\mathrm{jumps}} \rangle \lambda^2}$. By combining Eqs. (8) and (9), one obtains for the time until an oxygen vacancy is trapped by a Cu substitutional

$$t_{\mathrm{random\ walk}} = e^{(E_{\mathrm{barrier}}/k_B T)} / (p_{\mathrm{Cu}} N_{\mathrm{NN}} \nu_a f). \tag{10}$$

Whereas in the cubic, paraelectric phase at high temperature, which occurs during and directly after sintering a ferroelectric ceramic, all bound states are equivalent, in the ferroelectric phases there is an energetically preferred orientation of the defect complex with respect to the surrounding polarization. Those bound oxygen vacancies, which are not coincidentally already located in the lowest-energy position, are driven to move there. The time needed for this process is governed by the energy barrier for that jump:

$$t_{\mathrm{reorient}} = e^{(E_{\mathrm{barrier}}/k_B T)} / (N_{\mathrm{NN}} \nu_a f). \tag{11}$$

Assuming that jumps to an unbound position have a much higher energy barrier and are therefore negligible, here the number of possible final positions $N_{\mathrm{NN}}$ is 4 and $f = 0.6$.

In order to obtain an estimate for the energy barrier for the reorientation of the $Cu_{Nb}$-$V_O$ defect needed for Eq. (11), the DFT energy barrier for the migration of $V_O$ between nearest-neighbor lattice sites is determined by means of the "nudged elastic band" (NEB) algorithm[45] in simple-cubic $2 \times 2 \times 2$ supercells (40 atoms) at the theoretical lattice constant of undoped $KNbO_3$, assuming the charge state of the defect to be $(Cu_{Nb}\text{-}V_O)^-$ and that of the isolated O vacancy to be $V_O^{2+}$.

### C. Orthorhombic, ferroelectric $KNbO_3$ with defect complexes

#### 1. "Easy" and "hard" polarization directions (DFT and SMP)

In analogy to magnetocrystalline anisotropy, we call a direction of the spontaneous ferroelectric polarization $P$ "easy" if it is energetically favorable and "hard" if switching $P$ into this direction is energetically unfavorable. Cu-doped $KNbO_3$ in the orthorhombic ferroelectric phase is modeled using larger supercells with equal extensions in all Cartesian directions in order to account for the subtle energy differences between the different polarization states. The choice of unit cell is not unique. The simple cubic (sc) perovskite lattice can alternatively be represented by a face-centered-cubic (fcc) one, for which the lattice vectors in units of the simple-cubic ones read as [011], [101], and [110]. The fcc unit cell contains two formula units of $KNbO_3$, whereas the sc cell contains one (cf. Fig. 4). This change of unit cell allows for supercells with numbers of atoms different from those which can be obtained by multiplying the original sc unit cell. It is still possible when the structure is no longer exactly cubic, as in the orthorhombic phase we study here. When the sc unit cell of the paraelectric phase becomes a "simple-orthorhombic" (so) one in the ferroelectric phase, then the fcc cell becomes "face-centered orthorhombic" (fco). We use face-centered-orthorhombic (fco) $2 \times 2 \times 2$ supercells consisting of 16 perovskite unit cells (80 atoms), corresponding to a Cu concentration of 6.25 mol%.

For the DFT calculations of energy differences between easy and hard directions, plane waves with energies up to 340 eV in the basis and a $2 \times 2 \times 2$ Monkhorst-Pack[36] $k$ point for the orthorhombic supercell of $KNbO_3$ are used. With this choice, the density of $k$ points is nearly the same as that of a $5 \times 5 \times 5$ mesh for the single unit cell. The room-temperature phase of $KNbO_3$ has a base-centered orthorhombic conventional unit cell, but the primitive unit cell is monoclinic with $a < b = c$ and $\alpha < \beta = \gamma = 90^\circ$. For the sake of consistency, the theoretical equilibrium lattice parameters of undoped orthorhombic $KNbO_3$ are used ($a = 3.929$ Å, $b = c = 3.959$ Å) rather than the experimental ones. In order to reduce the number of cell parameters to be optimized in the DFT calculations, we fix the three angles of the primitive unit cell in the orthorhombic phase to 90° (experiment[12]: 90°; 90°; and 89.7°).

Whereas spin polarization is neglected when calculating the defect formation energies because its contribution is comparatively small in that case, the ferroelectric instabilities are so small that additional effects of spin polarization may make a difference. Therefore, we include it in the calculation of ferroelectric energy differences. However, we find that taking into account spin polarization has no significant effect on the energy differences between different ferroelectric configurations.

#### 2. *Switching between easy and hard polarization directions (SMP)*

The energy changes along transition paths between the different orientations of the ferroelectric polarization with respect to the defect complexes are calculated using a classical atomistic shell-model potential (SMP). In the shell model,[46] an atom is represented by an ionic core and an electronic shell, which interact with each other via a spring force,

$$V_{cs} = \frac{1}{2}k_1 r_{cs}^2 + \frac{1}{24}k_2 r_{cs}^4, \tag{12}$$

where $r_{cs}$ is the distance between core and shell. Cores and shells of different atoms interact with each other via the electrostatic Coulomb interaction, and the shells of different atoms interact additionally via the Buckingham[47] potential, which consists of a repulsive Born-Mayer[48] term and an attractive van der Waals term,

$$V_{ij}(r_{ij}) = A_{ij} e^{-\frac{r_{ij}}{\varrho_{ij}}} - \frac{C_{ij}}{r_{ij}^6}, \tag{13}$$

where $r_{ij}$ is the distance between two shells. The atomistic calculations are performed using the program GULP.[49] An atomistic potential for $KNbO_3$ from Ref. 50 with slightly modified parameters[51] is combined with a potential for a Cu-O interaction from Ref. 52. The potential parameters are compiled in Table I. The Buckingham potential is truncated at a distance of 6.5 Å, the spring force at 1 Å. This atomistic potential is first validated by calculating the energies of the different orientations of the ferroelectric polarization with respect to the defect complexes and comparing them to those obtained with DFT.

During the structure optimizations, symmetry constraints are applied both in the simulations with the SMP and in the DFT calculations. After validating the SMP, it is used to calculate the minimum-energy path for switching between the different polarization states by means of the NEB method. The NEB images are constructed by linear interpolation of initial and final configuration of the transition path. In cases where the lattice parameters differ between initial and final image structures (e.g., $a = b > c$ initially and $a < b = c$ finally), the lattice parameters are linearly interpolated and are kept constant. The atomic coordinates are optimized by the NEB method until the force norm $||f||$, defined as

$$||f|| = \frac{\sqrt{\sum_i f_i}}{N},$$

where $f_i$ is a force acting on an individual coordinate $x_i$ and $N$ is the number of coordinates, becomes less than about 1.5 meV/Å.

#### 3. *Ferroelectric polarization*

The ferroelectric polarization **P** is calculated as follows:

$$\mathbf{P} = \sum_i w_i \, Z_i \, e \, \Delta\mathbf{r}_i / V, \tag{14}$$

where $Z_i\, e$ is the charge of the $i$th particle in the supercell (core or shell, $e$ is the elementary charge quantum), $\Delta\mathbf{r}_i$ is its displacement vector from its ideal position in the paraelectric case, $V$ is the cell volume, and $w_i = 1/N_c$ is the weight factor of the atom in the (super)cell. It is equal to the reciprocal of the number of (super)cells $N_c$ the atom belongs to. In the DFT calculations, only the electric polarization of the ions is calculated, for which formal ionic charges ($K^+$, $Nb^{5+}$, $Cu^{2+}$, and $O^{2-}$) are assumed. The ferroelectric polarization obtained for this choice of reference state is that of the ferroelectric bulk plus the polarization induced by the defect dipole moment, but it does not include the bare defect dipole moment itself. The polarization obtained in this way is comparable to the polarization in the perfect crystal in the sense that in both cases it is zero if all atoms occupy the lattice sites of the paraelectric reference structure. When dipole moments of individual unit cells are calculated, the unit cells are centered in the $B$-site atom (Nb or Cu). In principle, in the case of DFT calculations, the polarization should be calculated using, e.g., the "Berry-phase approach" outlined in Refs. 53 and 54. However, it is a common practice (applied in, e.g., Refs. 55 and 56) to calculate instead the ferroelectric polarization of systems with distorted geometries (compared to the perfect crystal), such as domain walls or surfaces, by using an equation similar to our Eq. (14) with Born-effective charge tensors for the $Z_i$, which have been calculated for the perfect crystal. In the case of perfect, undoped $KNbO_3$ we find that the polarization obtained from Eq. (14) using formal charges and using a Born-effective charge tensor for cubic $KNbO_3$ from the literature[38] differ by a large, but approximately constant factor of about 1.8 (see Sec. III A). Because of this finding, and because Born-effective charges for the Cu-doped $KNbO_3$ are not available in the literature, we resort to formal charges when calculating dipole moments from defect structures obtained

TABLE I. Shell-model-potential parameters [cf. Eqs. (12) and (13)] for $Cu_{Nb}$-doped $KNbO_3$. Notice that for Cu atoms with $\infty$ for $k_1$ the core-shell polarization is turned "off."

| Atom | $A$ (eV) | $\varrho$ (Å) | $C$ (eVÅ$^6$) | Core charge ($e$) | Shell charge ($e$) | $k_1$ (eVÅ$^{-2}$) | $k_2$ (eVÅ$^{-4}$) |
|---|---|---|---|---|---|---|---|
| K | 126870.4000 | 0.194514 | 0.0 | 1.237854 | −0.418377 | 229.74443 | 0.0 |
| Cu | 712.8000 | 0.32698 | 0.0 | 0.000000 | 2.000000 | $\infty$ | 0.0 |
| Nb | 1053.2161 | 0.389027 | 0.0 | −2.984072 | 7.816735 | 255.95572 | 410.47927 |
| O | 3657.8642 | 0.282693 | 200.1785 | 1.122198 | −3.006245 | 76.581476 | 1539.2972 |

with DFT. However, the dipole moments obtained with formal ionic charges are only used for qualitative discussion purposes. In the case of the atomistic calculations with the shell model, the electronic contribution to the ferroelectric polarization arises from the electronic shells of the shell model, and the use of Born-effective charges is not required. Here, the core and shell charges of the SMP are used for the $Z_i$.

## III. RESULTS

### A. Validation of the computational methods and parameters

In Table II, the structural properties of undoped $KNbO_3$ obtained with the SMP and DFT are compared to experimentally measured ones. Our structure parameters obtained with the LDA at the theoretical volume are very similar to those obtained in Ref. 27 also with DFT, but for the experimental volume. Whereas in Ref. 27 a severe underestimation of the ferroelectric instabilities by the LDA for the theoretical volume is observed, we do not reproduce this discrepancy. Our results for ferroelectric instabilities, obtained with the LDA at the theoretical lattice constants, agree quantitatively well with data for heats of formation from experiment.[13] For a $5 \times 5 \times 5$ $k$-point mesh and a plane-wave cutoff energy of 300 eV for the single unit cell, which corresponds approximately to the parameters of our supercell calculations, the ferroelectric energy differences are not completely converged yet compared to an $8 \times 8 \times 8$ mesh and a cutoff energy of 340 eV, but agreement with experiment is similar in both cases.

In general, the SMP results are very close to the ones obtained with DFT. The atomic displacements $u_z$ in the ferroelectric phases with respect to those in the paraelectric case are underestimated by about one third both by the SMP and by DFT. The same is observed in Ref. 27 for different exchange-correlation functionals and may be related to the fact that the ferroelectric polarization and instabilities are extremely sensitive to slight changes in the volume of the unit cell. Using the atomic coordinates from DFT in Eq. (14), the ferroelectric polarization obtained with cubic Born-effective charges differs from the one obtained with formal ionic charges by an almost constant factor of about 1.8 for all phases of $KNbO_3$ considered here.

### B. Formation of defect complexes in cubic $KNbO_3$

#### 1. Defect formation energies

Figure 5 shows the defect formation energies of the $Cu_{Nb}$-$V_O$ complex and the straight $V_O$-$Cu_{Nb}$-$V_O$ complex as a function of the chemical potential of the electrons. The defect formation energies of the defect complexes (solid lines and filled symbols in Fig. 5) are lower than the sums of the defect formation energies of the isolated defects (dotted lines and open symbols in Fig. 5) by more than one eV. In the middle of the band gap, the binding energies are $E_B = -1.4$ eV for the $Cu_{Nb}$-$V_O$ defect and $E_B = -2.2$ eV for the straight $V_O$-$Cu_{Nb}$-$V_O$ defect. The formation energy of the bent $V_O$-$Cu_{Nb}$-$V_O$ defect obtained with DFT lies about 0.2 eV below that of the straight $V_O$-$Cu_{Nb}$-$V_O$ defect (not shown).

TABLE II. Structural properties (lattice constants $a$ and $c$, cell angle $\alpha$, bulk modulus $B$, volume $V$, ferroelectric instabilities with respect to the cubic phase $\Delta E_{FE}$ in meV/f.u., atomic displacements in the ferroelectric phases with respect to those in the paraelectric one in units of the lattice constant $u_z$) of undoped $KNbO_3$, and $z$ component of the ferroelectric polarization $P_z$ obtained with the SMP, DFT, and experiment (experimental values are taken from Refs. 12, 13, 22, 57, and 58). Numbers in brackets for the orthorhombic phase are those obtained for a monoclinic cell with $\alpha < \beta = \gamma = 90^\circ$. In the case of the SMP, the $u_z$ are those of the ionic cores. With DFT, $P_z$ is calculated once using formal charges (FC), once using Born-effective charges (BEC) from Ref. 38. The DFT calculations are, unless stated otherwise, performed for single perovskite unit cells, employing a $8 \times 8 \times 8$ $k$-point mesh and a plane-wave cutoff energy of 340 eV.

| Phase | | SMP | DFT | Expt. |
|---|---|---|---|---|
| Cubic | $a$ (Å) | 3.997 | 3.943 | 4.021 |
| | $V$ (Å$^3$) | 63.86 | 61.72 | 65.01 |
| | $B$ (GPa) | 184 | 223 | 165 |
| | | | | 172 |
| Tetrag. | $a$ (Å) | 3.989 | 3.931 | 3.997 |
| | $c$ (Å) | 4.056 | 3.995 | 4.063 |
| | $c/a$ | 1.017 | 1.016 | 1.017 |
| | $\Delta E_{FE}$ | −9.8 | −12.3 | −8.2 |
| | | | −6.6[a] | |
| | $u_z$ (K) | 0.016 | 0.012 | 0.023 |
| | $u_z$ (Nb) | 0.000 | 0.000 | 0.000 |
| | $u_z$ ($O_{1,2}$) | 0.040 | 0.034 | 0.042 |
| | $u_z$ ($O_3$) | 0.037 | 0.034 | 0.040 |
| | $P_z$ ($\mu$C/cm$^2$) | 26.9 | 20.0 (FC) | 30 (Ref. 22) |
| | | | 27.5 (BEC) | 37 (Ref. 58) |
| | | | 36.7 (BEC)[b] | |
| Orthorh. | $a$ (Å) | 3.986 (3.986) | 3.929 | (3.973) |
| | $c$ (Å) | 4.027 (4.028) | 3.959 | (4.036) |
| | $c/a$ | 1.011(1.011) | 1.010 | (1.017) |
| | $\alpha$ (degrees) | 90[c] (89.65) | 90[c] | (89.74) |
| | $\Delta E_{FE}$ | −11.4 | −13.5 | (−11.9) |
| | | | −8.9[a] | |
| | $u_z$ (K) | 0.006 | 0.010 | (0.016) |
| | $u_z$ (Nb) | 0.000 | 0.000 | (0.000) |
| | $u_z$ ($O_{1,2}$) | 0.022 | 0.024 | (0.028) |
| | $u_z$ ($O_3$) | 0.025 | 0.027 | (0.030) |
| | $P_z$ ($\mu$C/cm$^2$) | 20.2 | 14.4 (FC) | (22) (Ref. 22) |
| | | | 26.2 (BEC)[b] | (29) (Ref. 58) |
| Rhomboh. | $a$ (Å) | 4.015 | 3.952 | 4.016 |
| | $\alpha$ (degrees) | 89.74 | 89.91 | 89.83 |
| | $\Delta E_{FE}$ | −12.9 | −13.9 | −13.3 |
| | | | −9.1[a] | |
| | $u_z$ (K) | 0.005 | 0.008 | 0.0112 |
| | $u_z$ (Nb) | 0.000 | 0.000 | 0.0000 |
| | $u_z$ ($O_{1,2}$) | 0.020 | 0.021 | 0.0295 |
| | $u_z$ ($O_3$) | 0.018 | 0.021 | 0.0308 |
| | $P_z$ ($\mu$C/cm$^2$) | 17.3 | 12.0(FC) | |
| | | | 17.3 (BEC) | |
| | | | 21.9 (BEC)[b] | |

[a]Calculated with a $5 \times 5 \times 5$ $k$-point mesh and a plane-wave cutoff energy of 300 eV.
[b]Born-effective charges for the cubic phase were used.
[c]This angle was set to 90° and not varied.

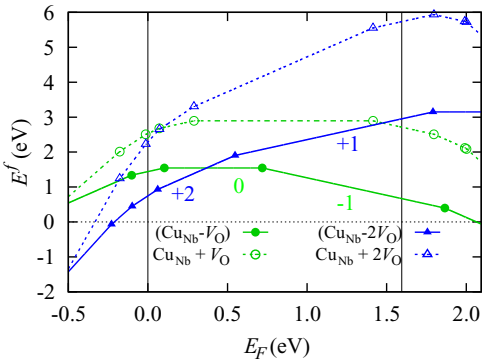


FIG. 5. (Color online) Formation energies $E^f$ of the defect complexes ($Cu_{Nb}$-$V_O$) and straight ($V_O$-$Cu_{Nb}$-$V_O$) as function of the Fermi energy $E_F$ in $KNbO_3$, as well as the sums of the formation energies of $Cu_{Nb}$ and one isolated $V_O$ ($Cu_{Nb} + V_O$) and two isolated $V_O$ ($Cu_{Nb} + 2V_O$). The electronic chemical potential ($E_F$) is allowed to vary between the LDA valence band maximum (VBM, $E_F = 0$) and conduction band minimum (CBM, $E_F = 1.59$ eV), as indicated by vertical lines. The numbers attached to the curves mark the charge states of the defects.

For the supercell we used for the cubic phase, the monopole-monopole energy [the second term in Eq. (7)] of a point defect with charge $2e$ (e.g., $V_O$ in its formal ionic charge state $+2e$) is only about 3 meV, whereas the dipole-dipole energy (the third term) of a dipole consisting of two point charges $\pm 2e$ separated by half a lattice constant, corresponding to the $Cu_{Nb}$-$V_O$ defect dipole, is zero. The straight $V_O$-$Cu_{Nb}$-$V_O$ defect complex does not have a dipole moment.

#### 2. *Time scales for the formation of defect complexes*

Figure 6 shows the energy barrier for the migration of a $V_O$ between two sites that are nearest neighbors of a $Cu_{Nb}$ substitutional. Hence, this is the energy barrier for rotating the $Cu_{Nb}$-$V_O$ defect by 90°. The DFT energy barrier amounts to 2 eV and is much higher than the energy barrier for the migration of an isolated $V_O$ along the same path, for which about 0.6 eV is obtained.

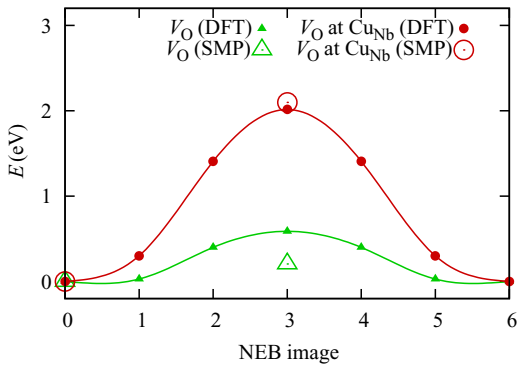


FIG. 6. (Color online) Energy barriers for the migration of an isolated $V_O$ and of a $V_O$ neighboring a $Cu_{Nb}$ substitutional. The latter corresponds to a rotation of the $Cu_{Nb}$-$V_O$ defect by 90°. The lines only serve as a guide to the eye.

At 300 K, from Eq. (10) one obtains $t_{\text{random walk}} = 0.3$ s, hence the oxygen vacancies have enough time to reach the Cu substitutionals. It is therefore reasonable to assume that a large fraction of the Cu substitutionals trap one or two oxygen vacancies immediately and no aging is required in order to obtain defect complexes. However, the rotation of the $Cu_{Nb}$-$V_O$ defect complex and hence the alignment of this defect complex with the surrounding polarization occurs on a different time scale. At a temperature of 708 K, which is near the Curie temperature (near the cubic-tetragonal transition), using Eq. (11), the time $t_{\text{reorient}}$ needed to spontaneously reorient the defect dipole is on the order of minutes only (we obtain 79 s). But, near the tetragonal-orthorhombic phase transition at 498 K it is prohibitively large (we obtain 30 months). Assuming that the barrier is reduced by about 0.1 eV due to its asymmetry in the orthorhombic phase, and by another 0.2 eV due to thermal expansion, with $E_{\text{barrier}} = 1.7$ eV a time of the order of a day (we obtain 20 h) is still needed to reorient this defect dipole at 498 K.

To further evaluate the ability of the SMP to reproduce DFT energies, the energy barriers are recalculated with the SMP by a symmetry-constrained energy minimization of the structures at the initial and the saddle points obtained with DFT. The SMP energy barriers amount to 0.2 eV (isolated $V_O$) and 2.1 eV ($V_O$ at $Cu_{Nb}$) (see open symbols in Fig. 6). The SMP strongly underestimates the energy barrier for jumps of the isolated $V_O$, but correctly predicts a much higher energy barrier for the bound $V_O$. Notice that apart from this one test, the SMP was not used for atomic jumps between lattice sites. It was employed to interpolate the DFT energy surface only where very small atomic displacements related to the ferroelectric polarization were involved (few percent of lattice constants, cf. Table II).

### C. Orthorhombic, ferroelectric $KNbO_3$ with defect complexes

#### 1. *Easy and hard polarization directions*

The energies of the different inequivalent orientations of $P$ with respect to the defect complexes in Fig. 2 obtained with DFT and with the SMP are depicted in Fig. 7. For all three defect complexes, the energy of the system is lowest if $P$ forms the smallest possible angle with the defect axis $A_D$. If the defect complex has an electric dipole moment $P_D$, as in the cases of the $Cu_{Nb}$-$V_O$ defect and the bent $V_O$-$Cu_{Nb}$-$V_O$ defect, for a given angle between $P$ and $A_D$ the energy is lowest for the configuration with the smallest possible angle between $P_D$ and $P$. Spin polarization does not have an effect on the energy differences between different orientations of the ferroelectric polarization (see filled and open black circles in Fig. 7).

In the orthorhombic phase, the monopole-monopole energy of the point charge $2e$ is 60 meV, the dipole-dipole energy of the formally charged $[Cu_{Nb}^{3-}\text{-}V_O^{2+}]^{1-}$ defect is 23 meV (it is repulsive) if it has a component parallel or antiparallel to the electric polarization, and about 5 meV for the orthogonal orientation (in this case it is attractive). For the formally charged $[Cu_{Nb}^{3-}\text{-}2V_O^{2+}]^{1+}$ defect, the dipole-dipole energy is repulsive for all orientations studied here. It is 86 meV if the defect has a component orthogonal to the polarization, and 140 meV if it is parallel or antiparallel to the polarization. Therefore, a dipole-dipole correction would further stabilize

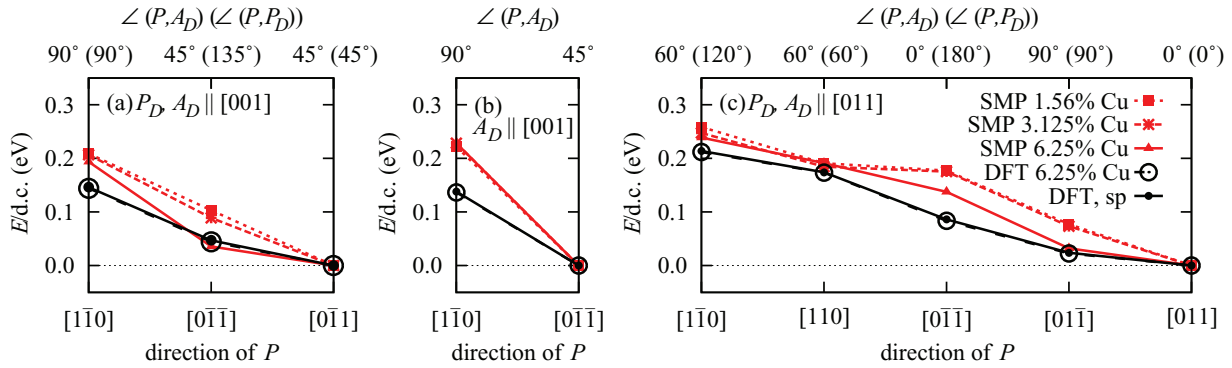


FIG. 7. (Color online) Potential energy per Cu defect complex (d.c.) of the configurations depicted in Fig. 2. (a) $Cu_{Nb}$-$V_O$; (b) straight $V_O$-$Cu_{Nb}$-$V_O$; (c) bent $V_O$-$Cu_{Nb}$-$V_O$. Black solid lines and circles: DFT; red lines and symbols: SMP. Small filled and large open circles in (a)–(c): DFT calculations with and without spin polarization, respectively. The lines only serve as a guide to the eye.

the parallel orientation of defect dipole moment and ferroelectric polarization.

The SMP reproduces the order of the energies correctly, although it overestimates the energy difference between the bent and the straight $V_O$-$Cu_{Nb}$-$V_O$ defect (SMP: 1.3 eV; DFT: 164 meV). As long as only small atomic displacements are involved, such as during the rotation of the ferroelectric polarization, the SMP results agree qualitatively and semiquantitatively with those obtained with DFT, so that we proceed with the SMP in the following.

### 2. *Switching between easy and hard polarization directions*

By means of the NEB method, the energy changes along transition paths between different relative orientations of $P$ and the defect complexes are calculated with the SMP for different defect concentrations, ranging from 6.25 mol%, for which the DFT calculations were performed as well, to approximately 1.5 mol% Cu (one Cu defect in a 320-atom supercell). In Fig. 8, the Cartesian components of the ferroelectric polarization and the potential energy (per Cu defect and per perovskite formula unit, respectively) along several paths for homogeneous switching in a crystal region with a $Cu_{Nb}$-$V_O$ defect are depicted. For a Cu concentration of 6.25 mol%, the ferroelectric polarization of the configurations $[0\bar{1}\bar{1}]$ and $[\bar{1}0\bar{1}]$ (here, the $z$ component of $P$ is oriented antiparallel to $P_D$) is strongly perturbed by the defect complex [see open circles in Fig. 8(a)], but for the two lower Cu concentrations [cross and star symbols in Fig. 8(a)] it converges toward the bulk value. The energy barrier between the configurations $[\bar{1}0\bar{1}]$ and $[\bar{1}01]$ is comparatively small with respect to the energy differences between different equilibrium configurations. Whereas the energy differences per defect between the different relative orientations of $P$ are approximately constant as expected [Fig. 8(b)], the energy barrier between the configurations $[\bar{1}0\bar{1}]$ and $[\bar{1}01]$ is also approximately constant and does not yet converge to the bulk value for the Cu concentrations studied here. The well-converged energies per defect complex indicate that the defect concentration is low enough to avoid finite-size effects. Therefore, the difference between energy barriers in the doped and the undoped case occurs more likely because the defects break the symmetry of the perfect orthorhombic crystal structure. Hence, in the supercell with the defect more and different intermediate configurations are possible than in the single, perfect unit cell under symmetry constraints.

Figure 9 shows the corresponding results for the straight $V_O$-$Cu_{Nb}$-$V_O$ defect complex. The energy differences between the equilibrium configurations $[1\bar{1}0]$, $[0\bar{1}\bar{1}]$, $[0\bar{1}1]$, and $[101]$ are apparently converged with respect to the Cu concentration [cf. Fig. 9(b)], whereas in this case also the energy barrier between the configurations $[0\bar{1}\bar{1}]$ and $[0\bar{1}1]$ converges smoothly to the bulk value [cf. Fig. 9(c)].

Figure 10 shows the corresponding results for the bent $V_O$-$Cu_{Nb}$-$V_O$ defect. Again, the energy difference per defect complex [Fig. 10(b)] is approximately converged with respect to the defect concentration, whereas the energy barriers for switching between the equilibrium configurations do not yet approach their bulk values for the concentrations studied here

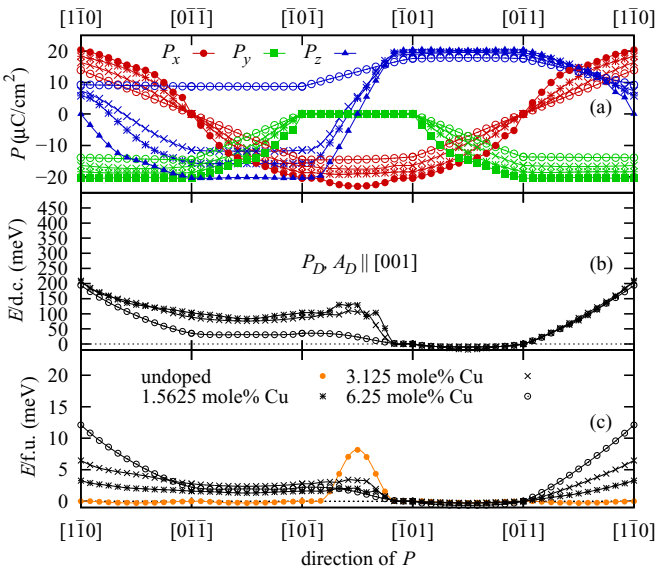


FIG. 8. (Color online) (a) Polarization, (b) potential energy per Cu defect complex (d.c.), and (c) potential energy per perovskite formula unit (f.u.) along transition paths in $KNbO_3$ with a $Cu_{Nb}$-$V_O$ defect complex [see Fig. 2(a)]. The lines only serve as a guide to the eye.

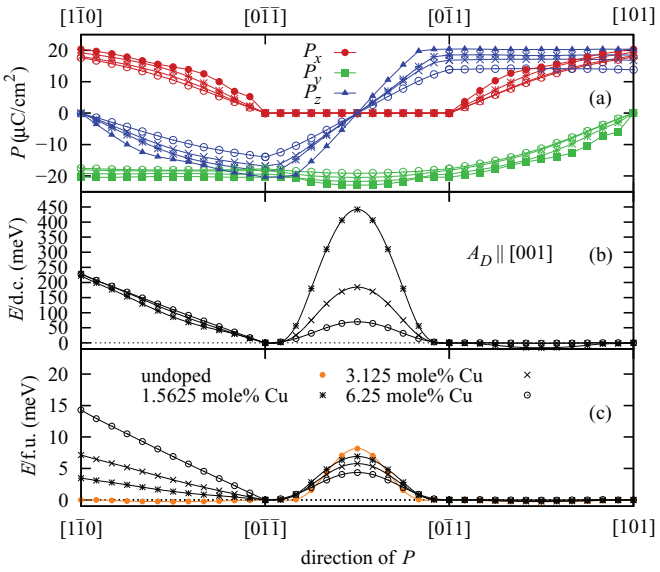


FIG. 9. (Color online) The same as in Fig. 8 for the straight $V_O$-$Cu_{Nb}$-$V_O$ defect [see Fig. 2(b)].

[Fig. 10(c)]. The fact that the energy barriers converge well for the straight $V_O$-$Cu_{Nb}$-$V_O$ defect, but not for the $Cu_{Nb}$-$V_O$ defect and the bent $V_O$-$Cu_{Nb}$-$V_O$ defect, is probably related to the lower symmetries of the latter two defects with respect to the former one and the undoped crystal.

Figure 11 illustrates the atomic positions and the ionic polarization around a $Cu_{Nb}$-$V_O$ defect complex for the configurations $P \uparrow\uparrow P_D$, $P \uparrow\downarrow P_D$, and $P \perp P_D$ after energy minimization with DFT. The configuration depicted in Fig. 11 is obtained by periodically replicating the face-centered-orthorhombic supercell (79 atoms) used for the DFT calculations and then cutting out a plane which contains the defect complex. The neighboring Nb and Cu ions move away from $V_O$, which in the case of $P \uparrow\downarrow P_D$ leads to polarization reversal in the unit cells numbered 2 and 8 with respect to the surrounding $P$.

## IV. DISCUSSION

The formation of the defect complexes is associated with an energy gain of more than 1 eV (cf. Fig. 4), hence the defect complexes will actually form. Since the time a $Cu_{Nb}$ substitutional needs to trap a $V_O$ is very short even at room temperature (we obtain 0.3 s), and even much shorter at elevated temperatures, the defect complexes form instantaneously, and no aging is required. But once formed, the defect complexes align with the surrounding ferroelectric polarization much more slowly (estimated in some days even at elevated temperatures) because the energy barrier for reorienting the $Cu_{Nb}$-$V_O$ defect dipole is high, although we are aware that our calculated estimate of 2 eV for the energy barrier (cf. Fig. 6) may be not yet converged with respect to the supercell size. In principle, this energy barrier should be calculated for the orthorhombic phase of $KNbO_3$, and one would obtain an asymmetric barrier, analogous to the approach that was made in Ref. 59 for $Fe_{Ti}$-$V_O$ defect complexes in tetragonal $PbTiO_3$. However, the minimum energy path in Fe-doped $PbTiO_3$ is very asymmetric and attains barrier values of either about 0.2 or about 1.2 eV, depending on the direction of the jump, which is caused by the large energy differences between the different positions of the $V_O$ with respect to $P$ there. In the case of Cu-doped $KNbO_3$, the corresponding energy differences are very small compared to the energy barrier itself (about 0.2 eV compared to 2 eV), so that here, unlike in $PbTiO_3$, the asymmetry of the minimum energy path is much smaller and can be neglected as a first approximation. Since the energy barrier for rotating the $Cu_{Nb}$-$V_O$ defect dipole (≈2 eV, cf. Fig. 6) is much higher than the one for rotating the surrounding polarization (≈0.2 eV, cf. Fig. 8), the defect

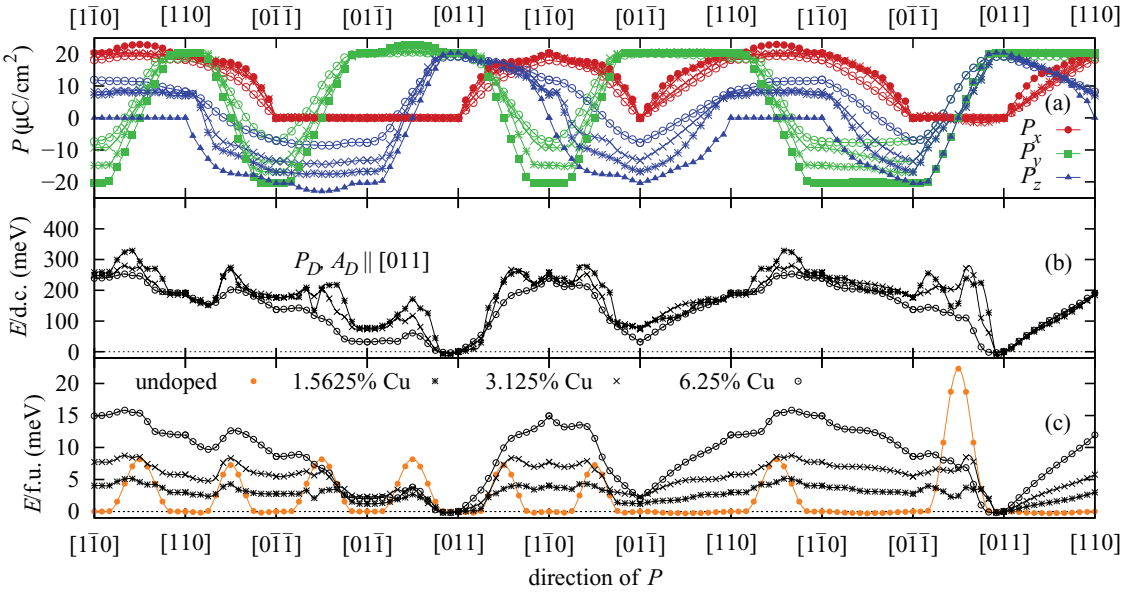


FIG. 10. (Color online) The same as in Fig. 8 for the bent $V_O$-$Cu_{Nb}$-$V_O$ defect [see Fig. 2(c)].

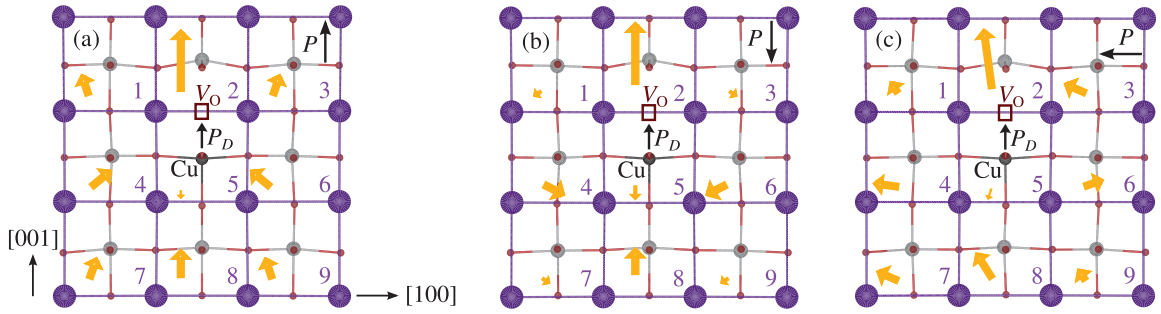


FIG. 11. (Color online) Atomic positions (large purple spheres: K, medium gray spheres: Nb, medium black sphere: Cu, small red spheres: O) near a $Cu_{Nb}$-$V_O$ defect complex [see Fig. 2(a)] for the configurations (a) $P \uparrow\uparrow P_D$, (b) $P \uparrow\downarrow P_D$, and (c) $P \perp P_D$ after energy minimization with DFT. Orange arrows mark the electric dipole moments of the individual unit cells.

dipole will remain immobile in an external ac field. Artificial interactions between periodic images of the defects in the calculations are small due to the large dielectric constant of this material. Finite-size effects should be even smaller for the migration barriers than for the defect formation energies because charge corrections are to some extent the same for the different configurations along the migration path (e.g., the electrostatic monopole-monopole interaction is the same for all NEB images).

We now compare the alignment behavior of $P$ and $P_D$ in Cu-doped $KNbO_3$ to that in Fe- or Cu-doped $PbTiO_3$, which has been investigated earlier in Ref. 60. There it has been found for the defect complexes $Cu_{Ti}$-$V_O$ and $Fe_{Ti}$-$V_O$ in tetragonal $PbTiO_3$ that the configuration $P \uparrow\uparrow P_D$ is lowest in energy. Whereas in Ref. 60 the configuration $P \perp P_D$ of the $Fe_{Ti}$-$V_O$ defect complex has the highest energy, like the $Cu_{Nb}$-$V_O$ and the bent $V_O$-$Cu_{Nb}$-$V_O$ defect in $KNbO_3$ as obtained in this work, for the $Cu_{Ti}$-$V_O$ defect in $PbTiO_3$ the configuration with the highest energy is $P \uparrow\downarrow P_D$. The energy penalty for the configuration $P \uparrow\downarrow P_D$ in $PbTiO_3$ depends strongly on the dopant: For the $Cu_{Ti}$-$V_O$ defect it is 1.2 eV, whereas for the $Fe_{Ti}$-$V_O$ defect it is only 0.45 eV.[60] In $KNbO_3$ it is even smaller, for the $Cu_{Nb}$-$V_O$ and the bent $V_O$-$Cu_{Nb}$-$V_O$ defect it is only 0.15 and 0.21 eV, respectively. These energy penalties hence depend very sensitively on the dopant and the host crystal species.

Based on the results of our own DFT relaxation calculations and those of Erhart *et al.*,[60] that a $V_O$ repels the nearest $B$ cations in doped PZT and KNN (both host and dopant ions, $B$ stands for Ti, Nb, Cu, or Fe, cf. Fig. 11 for Cu-doped $KNbO_3$), we propose the following explanation for the energetic ordering of the configurations $P \uparrow\uparrow P_D$, $P \uparrow\downarrow P_D$, and $P \perp P_D$:

In the ground state ($P \uparrow\uparrow P_D$), two stability conditions are fulfilled. First, the defect axis is oriented along the direction of the ferroelectric strain (which is parallel to $P$). This condition is fulfilled for either $P \uparrow\uparrow P_D$ or $P \uparrow\downarrow P_D$. The second stability condition is that $P \uparrow\uparrow P_D$ (and not $P \uparrow\downarrow P_D$). The first condition, the parallel alignment of defect axis and strain, allows us to accommodate the large displacements of the nearest $B$ ions away from $V_O$, the second condition enables the ferroelectric polarization to have the same direction in all unit cells, only perhaps with the exception of the cell containing the substitutional $B$ atom. More precisely, as can be seen in Fig. 11, the unit cell containing the substitutional acceptor atom (the unit cell no. 5 in Fig. 11) does not contribute much to the overall ferroelectric polarization, whereas a strong contribution arises from the unit cell which contains a host $B$ atom and $V_O$ (unit cell no. 2 in Fig. 11). Due to the large displacement of the $B$ ion, the individual polarization of unit cell no. 2 is always parallel $P_D$, regardless of the overall direction of $P$ in the surrounding unit cells. In the case $P \uparrow\downarrow P_D$, therefore a minuscule ferroelectric "domain wall" is created (essentially around unit cell no. 2), which costs energy. Hence, the first condition minimizes the elastic strain energy, whereas the second minimizes the electrostatic energy. If the first condition dominates over the second, $P \uparrow\downarrow P_D$ is more stable than $P \perp P_D$, and vice versa.

In the case of Cu-doped $KNbO_3$ the main effect of the defect complexes is that they create "easy" and "hard" directions for $P$ and are thus responsible for hardening mechanism (1), whereas the energy barriers for polarization switching created by the defects are usually small in comparison to the energy differences between easy and hard directions, so that hardening mechanism (2) is less relevant in the case of Cu-doped $KNbO_3$.

The combination of moderately small energy differences between easy and hard ferroelectric polarization directions and very low-energy barriers for switching between these, which we find for Cu-$V_O$ and $V_O$-Cu-$V_O$ defect complexes in $KNbO_3$, mean that these defect complexes can provide a restoring force for $P$. Hence, these defect complexes should enable the reversible 90° domain switching mechanism. However, because the energy differences between different orientations of the defect complexes with respect to the surrounding polarization found here are much smaller than those found for Cu- and Fe-doped $PbTiO_3$ in Ref. 60, this effect should be smaller in Cu-doped $KNbO_3$ than in Cu- or Fe-doped $PbTiO_3$.

In a previous study of Cu-doped KNN, using a virtual-crystal approximation for the $A$-site species K and Na, we found very similar formation and binding energies (maximum 0.2-eV difference in defect formation energy) for the same defect complexes as studied here in $KNbO_3$.[61] Moreover, the crystal structure of KNN and the one of $KNbO_3$ are the same up to a Na content of 50%, and the lattice parameters evolve smoothly from $KNbO_3$ to $(K_{0.5},Na_{0.5})NbO_3$ in this composition region.[62] If therefore the ferroelectric energies in Cu-doped KNN vary smoothly with composition as well, our results obtained for $KNbO_3$ should be at least qualitatively transferable to KNN for compositions with not too high sodium content.

## V. SUMMARY

Three types of atomic defect complexes in Cu-doped $KNbO_3$, namely, the $Cu_{Nb}$-$V_O$ defect complex, a straight and a bent configuration of the $V_O$-$Cu_{Nb}$-$V_O$ defect complex, were investigated using density-functional theory and classical atomistic simulation. All three complexes create easy and hard directions for the ferroelectric polarization in the orthorhombic room-temperature phase of $KNbO_3$ and may thus contribute to ferroelectric hardening of this material. The energy differences between easy and hard directions, however, are small compared to those found in Ref. 60 for Cu- and Fe-doped $PbTiO_3$, so that the effect is expected to be smaller than in Cu- or Fe-doped $PbTiO_3$. The existence of easy and hard polarization directions, together with small energy barriers for polarization switching found here for Cu-doped $KNbO_3$, supports the assumption that one of these defect complexes or both of them are responsible for the reversible 90° domain switching observed experimentally in the isostructural (K,Na)$NbO_3$ when doped with Cu.

## ACKNOWLEDGMENTS

Financial funding for this work by the German Research Foundation (DFG, Grant No. EL 155/21-1,2) and computer resources provided by the High-Performance Computing Center of the University of Karlsruhe, Germany (HP XC4000), are gratefully acknowledged. We thank our project partners, especially E. Erünal and R.-A. Eichel, who found experimental evidence for such defect complexes in KNN and motivated us to investigate them theoretically.

*Present address: ILM, Université Claude Bernard Lyon I, 69622 Villeurbanne, France; sabine.korbel@univ-lyon1.fr
†christian.elsaesser@iwm.fraunhofer.de

[1] S. Zhang, R. Xia, and T. Shrout, J. Electroceram. **19**, 251 (2007).
[2] D. Damjanovic, in *The Science of Hysteresis*, edited by I. Mayergoyz and G. Bertotti (Elsevier, Amsterdam, 2005), Vol. 3.
[3] X. Ren, Nat. Mater. **3**, 91 (2004).
[4] Z. Feng and X. Ren, Phys. Rev. B **77**, 134115 (2008).
[5] D. Lin, K. W. Kwok, and H. L. Chan, Appl. Phys. Lett. **90**, 232903 (2007).
[6] X. Tan *et al.*, Mater. Res. Bull. **47**, 4472 (2012).
[7] G. Shirane, R. Newnham, and R. Pepinsky, Phys. Rev. **96**, 581 (1954).
[8] Y. Saito, H. Takao, and T. Tani *et al.*, Nature (London) **432**, 84 (2004).
[9] M. Matsubara, K. Kikuta, and S. Hirano, J. Appl. Phys. **97**, 114105 (2005).
[10] R. A. Eichel *et al.*, Appl. Phys. Lett. **102**, 242908 (2013).
[11] E. Erünal *et al.*, Funct. Mater. Lett. **3**, 19 (2010).
[12] A. W. Hewat, J. Phys. C: Solid State Phys. **6**, 2559 (1973).
[13] G. Shirane *et al.*, Phys. Rev. **93**, 672 (1954).
[14] J. Acker, H. Kungl, and M. Hoffmann, J. Am. Ceram. Soc. **93**, 1270 (2010).
[15] S. Körbel, P. Marton, and C. Elsässer, Phys. Rev. B **81**, 174115 (2010).
[16] C. Van de Walle and J. Neugebauer, J. Appl. Phys. **95**, 3851 (2004).
[17] K. Reuter and M. Scheffler, Phys. Rev. B **65**, 035406 (2001).
[18] *CRC Handbook of Chemistry and Physics*, 89th ed., edited by D. R. Lide (CRC Press, Boca Raton, FL, 2008).
[19] G. Makov and M. C. Payne, Phys. Rev. B **51**, 4014 (1995).
[20] L. N. Kantorovich, Phys. Rev. B **60**, 15476 (1999).
[21] C. Persson, Y.-J. Zhao, S. Lany, and A. Zunger, Phys. Rev. B **72**, 035211 (2005).
[22] S. Triebwasser, Phys. Rev. **101**, 993 (1956).
[23] S. T. Murphy and N. D. M. Hine, Phys. Rev. B **87**, 094111 (2013).
[24] R. Rurali and X. Cartoixà, Nano Lett. **9**, 975 (2008).
[25] E. Cancès, B. Mennucci, and J. Tomasi, J. Chem. Phys. **107**, 3032 (1997).
[26] E. Wiesendanger, Ferroelectrics **6**, 263 (1974).
[27] Z. Wu, R. E. Cohen, and D. J. Singh, Phys. Rev. B **70**, 104112 (2004).
[28] D. M. Ceperley and B. J. Alder, Phys. Rev. Lett. **45**, 566 (1980).
[29] J. P. Perdew and A. Zunger, Phys. Rev. B **23**, 5048 (1981).
[30] B. Meyer, F. Lechermann, C. Elsässer, and M. Fähnle, Fortran90 Program for Mixed-Basis Pseudopotential Calculations for Crystals, Max-Planck-Institut für Metallforschung, Stuttgart.
[31] C. Elsässer, N. Takeuchi, K. Ho, C. Chan, P. Braun, and M. Fähnle, J. Phys.: Condens. Matter **2**, 4371 (1990).
[32] K. Ho, C. Elsässer, C. Chan, and M. Fähnle, J. Phys.: Condens. Matter **4**, 5189 (1992).
[33] B. Meyer, K. Hummler, C. Elsässer, and M. Fähnle, J. Phys.: Condens. Matter **7**, 9201 (1995).
[34] F. Lechermann, F. Welsch, C. Elsässer, C. Ederer, M. Fähnle, J. M. Sanchez, and B. Meyer, Phys. Rev. B **65**, 132104 (2002).
[35] D. Vanderbilt, Phys. Rev. B **32**, 8412 (1985).
[36] H. J. Monkhorst and J. D. Pack, Phys. Rev. B **13**, 5188 (1976).
[37] C. L. Fu and K. M. Ho, Phys. Rev. B **28**, 5480 (1983).
[38] C.-Z. Wang, R. Yu, and H. Krakauer, Phys. Rev. B **54**, 11161 (1996).
[39] P. Erhart, P. Träskelin, and K. Albe, Phys. Rev. B **88**, 024107 (2013).
[40] R. Lohkämper, H. Neumann, and G. Arlt, J. Appl. Phys. **68**, 4220 (1990).
[41] A. Einstein, Ann. Phys. (Berlin, Ger.) **322**, 549 (1905).
[42] *Kinetics of Materials*, edited by R. Balluffi, S. Allen, W. Carter, and R. Kemper (Wiley, Hoboken, NJ, 2005).
[43] P. Erhart and K. Albe, J. Appl. Phys. **102**, 084111 (2007).
[44] M. Fontana *et al.*, J. Phys. C: Solid State Phys. **17**, 483 (1984).
[45] G. Henkelman, B. P. Uberuaga, and H. Jonsson, J. Chem. Phys. **113**, 9901 (2000).
[46] B. G. Dick and A. W. Overhauser, Phys. Rev. **112**, 90 (1958).
[47] R. A. Buckingham, Proc. R. Soc. London, Ser. A **168**, 264 (1938).
[48] M. Born and J. E. Mayer, Z. Phys. **75**, 1 (1932).
[49] J. D. Gale and A. L. Rohl, Mol. Simul. **29**, 291 (2003).
[50] M. Sepliarsky, A. Asthagiri, S. Phillpot, M. Stachiotti, and R. Migoni, Curr. Opin. Solid State Mater. Sci. **9**, 107 (2005).
[51] S. Körbel and C. Elsässer, Phys. Rev. B **84**, 014109 (2011).
[52] R. Baetzold, J. Am. Ceram. Soc. **73**, 3185 (1990).
[53] R. D. King-Smith and David Vanderbilt, Phys. Rev. B **47**, 1651 (1993).
[54] R. Resta, Rev. Mod. Phys. **66**, 899 (1994).

[55]G. Pilania and R. Ramprasad, Phys. Rev. B **82**, 155442 (2010).
[56]B. Meyer and D. Vanderbilt, Phys. Rev. B **65**, 104111 (2002).
[57]J. C. Chervin, J. P. Itie, D. Gourdain, and P. Pruzan, Solid State Commun. **110**, 247 (1999).
[58]W. Kleemann, F. J. Schäfer, and M. D. Fontana, Phys. Rev. B **30**, 1148 (1984).
[59]P. Marton and C. Elsässer, Phys. Rev. B **83**, 020106(R) (2011).
[60]P. Erhart, R.-A. Eichel, P. Träskelin, and K. Albe, Phys. Rev. B **76**, 174116 (2007).
[61]S. Körbel, Ph.D. thesis, Albert-Ludwigs-Universität Freiburg, 2012; www.freidok.uni-freiburg.de/volltexte/8860/pdf/diss.pdf
[62]D. W. Baker, P. A. Thomas, N. Zhang, and A. M. Glazer, Appl. Phys. Lett. **95**, 091903 (2009).